Materials & Design 225 (2023) 111470

Contents lists available at ScienceDirect

Materials & Design

journal homepage: www.elsevier.com/locate/matdes

Laves phases in Mg-Al-Ca alloys and their effect on mechanical properties

Muhammad Zubair [a,b,1,*], Markus Felten [c,1], Bengt Hallstedt [d,*], Miquel Vega Paredes [e], Lamya Abdellaoui [e], Ruben Bueno Villoro [e], Marta Lipinska-Chwalek [f,g], Nadia Ayeb [h], Hauke Springer [e,h], Joachim Mayer [f,g], Benjamin Berkels [i], Daniela Zander [c], Sandra Korte-Kerzel [a], Christina Scheu [e], Siyuan Zhang [e,*]

[a] Institute for Physical Metallurgy and Materials Physics, RWTH Aachen University, 52074 Aachen, Germany
[b] Department of Metallurgical & Materials Engineering, Faculty of Chemical, Metallurgical & Polymer Engineering, University of Engineering & Technology (UET) Lahore, Pakistan
[c] Chair of Corrosion and Corrosion Protection, RWTH Aachen University, Aachen, Germany
[d] Institute for Materials Applications in Mechanical Engineering, RWTH Aachen University, 52062 Aachen, Germany
[e] Max-Planck-Institut für Eisenforschung, Max-Planck-Str. 1, 40237 Düsseldorf, Germany
[f] Central Facility for Electron Microscopy, RWTH Aachen University, 52074 Aachen, Germany
[g] Ernst Ruska-Centre for Microscopy and Spectroscopy with Electrons (ER-C), 52428 Forschungszentrum Jülich, Germany
[h] Metallic Composite Materials, RWTH Aachen University, 52072 Aachen, Germany
[i] Aachen Institute for Advanced Study in Computational Engineering Science (AICES), RWTH Aachen University, Schinkelstraße 2, 52062 Aachen, Germany

HIGHLIGHTS

- Laves phases are designed in Mg-Al-Ca alloys in three crystal structures, as interconnected networks and dispersed particles depending on the heat treatment.
- The Laves phases in equilibrium with Mg matrix have composition in agreement with Calphad modelling. New compositional ranges of Laves phases were determined from non-equilibrium microstructures.
- Semi-coherent and incoherent interfaces between Laves phases and the Mg matrix were revealed by high resolution electron microscopy.
- The ductility of the alloys is significantly improved by annealing. Their yield strengths depend on the interconnectivity and inter-particle spacing of the Laves phases.

GRAPHICAL ABSTRACT

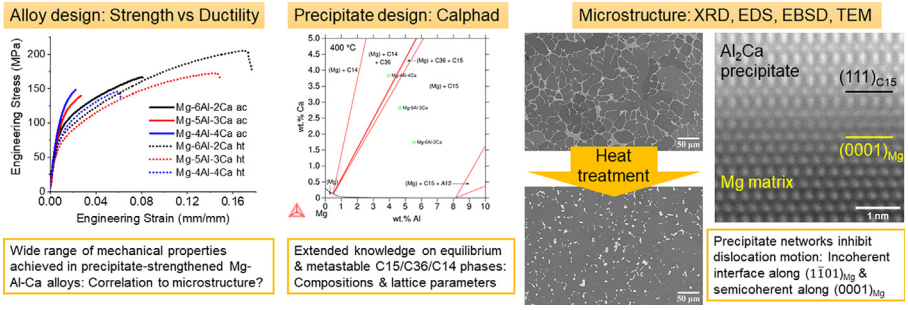

ARTICLE INFO

Article history:
Received 3 September 2022
Revised 25 November 2022
Accepted 5 December 2022
Available online 6 December 2022

ABSTRACT

Mg-Al-Ca alloys with Laves phase reinforcement are suitable for structural applications. The composition, crystal structure, and distribution of Laves phases can be tuned by the alloy composition and heat treatment, which subsequently influence their mechanical properties. In this study, three model alloys Mg-6Al-2Ca, Mg-5Al-3Ca and Mg-4Al-4Ca were investigated, which include C15, C36, and C14 Laves phases. The as-cast alloys have interconnected Laves phases that form a skeleton structure. After annealing, they

* Corresponding authors at: Max-Planck-Institut für Eisenforschung, Max-Planck-Str. 1, 40237 Düsseldorf, Germany (S. Zhang).
E-mail addresses: zubair@uet.edu.pk (M. Zubair), b.hallstedt@iwm.rwth-aachen.de (B. Hallstedt), siyuan.zhang@mpie.de (S. Zhang).
[1] These authors contributed equally to this work.

https://doi.org/10.1016/j.matdes.2022.111470
0264-1275/

Keywords:
Laves phase
Orientation relationship
Precipitate strengthening
Aberration-corrected electron microscopy
Calphad modelling

became more rounded particles, while the metastable C36 phase was transformed to C15. The Laves phases in different crystal structures exhibit distinct ranges of chemical compositions and lattice parameters. Well defined orientation relationships were observed between small C15 platelets and the Mg matrix (Mg(0002) // C15(1 1 1), Mg[11$\bar{2}$0] // C15[11$\bar{2}$]). Another pair of parallel orientations was found between Mg(11$\bar{0}$1) and the *c*-plane of hexagonal C36/C14. Nevertheless, most coarsened Laves phases have incoherent interfaces with the matrix and hinder dislocation slip transfer. The annealed alloys have lower yield strength than their as-cast counterparts, but higher ductility or ultimate tensile strength. The yield strengths of as-cast alloys are correlated to the interconnectivity of the skeleton, whereas those of annealed alloys are related to the spacing between Laves phases.

1. Introduction

Mg alloys have been increasingly applied in lightweight structural systems owing to their low density. Al is the most common alloying element in Mg alloys to improve the hardness, specific strength and corrosion resistance [1]. Ca addition to Mg-Al alloys results in grain refinement, improved thermal stability [2], and increased creep resistance [3–5]. Mg-Al-Ca alloys with Al and Ca contents exceeding their solubility limit have a dual phase microstructure, comprising of a hexagonal close packed (HCP) Mg matrix strengthened by Laves phases [6–8].

Laves phases with AB_2 stoichiometry form one of the most prominent classes of intermetallic compounds. Metal combinations from nearly the entire periodic table can form Laves phases [8–13]. Most Laves phase compounds have high strength and limited ductility, which is attributed to their tightly packed crystal structure comprising of quadruple layers [9,10,13–15]. Depending on the stacking sequence of the quadruple layers, Laves phases are further classified into three different crystal structures, C14, C15, and C36, with 2H, 3C, and 4H stacking, respectively [9,15].

With increasing Ca/Al ratio from 0 to 1, the type of secondary phases changes from $Mg_{17}Al_{12}$ (A12) to the Laves phases Al_2Ca (C15), $(Mg,Al)_2Ca$ (C36) and Mg_2Ca (C14) [2,16–20]. With increasing Ca/Al ratio, the Laves phases become more interconnected and form a skeleton structure [16,21], leading to enhanced creep resistance [3,4,21]. However, higher interconnectivity of the skeleton structure also results in reduction of ductility, as cracks tend to nucleate and grow preferably along the Laves phase skeleton [16,21,22] under loading. The most suitable alloy compositions for high temperature applications comprise the range of Ca/Al = 0.2–1.0, containing predominantly the C36 Laves phase [5,21,23–25]. However, C36 is metastable at low temperature [26,27] and was reported to transform to C15 during aging at 300 °C [26].

The bulk intermetallic phases $Mg_xAl_{2-x}Ca$ have been well studied in literature [28,29]. With increasing *x* from 0 to 2, they adopt different crystal structures from C15, C36, to C14 Laves phases. Compared to their bulk intermetallic form, less is known for these Laves phases as secondary phases in Mg alloys. Indeed, the small size (~1 μm) of Laves phases in Mg-Al-Ca alloys makes it challenging to determine the precise phase and composition via conventional analytical methods. Moreover, to resolve their interface and orientation relationship (OR) with the Mg matrix, transmission electron microscopy (TEM)-based characterization needs to be employed [6,23,24,30]. Several recent studies have reported plasticity in Laves phases [6,30–34]. To explore transfer of plasticity across the Mg/Laves phase interfaces, it is essential to understand the OR between the two phases [30].

In this article, the Laves phases with C15, C36, and C14 structures have been systematically studied in Mg-Al-Ca alloys with three compositions. To facilitate the study on the OR between Laves phases and Mg matrix, the as-cast skeleton microstructure was coarsened by annealing at 500 °C, close to the solidus temperature. X-ray diffraction (XRD) was applied to study the crystal structure and lattice parameter of the Laves phases. The morphology of Laves phases was analysed by scanning electron microscopy (SEM), whereas their phase composition and OR were respectively characterized by energy dispersive X-ray spectroscopy (EDS) and electron backscattered diffraction (EBSD). Selected interfaces with well-defined ORs were further resolved by high resolution TEM. The three alloys in the as-cast and heat-treated states exhibit different mechanical properties, which is rationalized based on the comprehensive analysis on their microstructure.

2. Experimental

The raw materials were melted in a steel crucible using a vacuum induction melting system under a protective Ar atmosphere at 0.8 bar. Casting was performed inside the furnace in a Cu mould with 10 mm wall thickness and an internal cross section of 25 × 65 mm^2, where the samples were kept until cooling to room temperature. Compositions were measured via wet chemical analysis and are listed in Table 1. The as-cast (Mg-*x*Al-*y*Ca ac) samples were subsequently annealed in a protective Ar atmosphere at 500 °C for 48 hr, and then slowly cooled down within the furnace with a cooling rate of 100 °C/hr. The heat-treated samples are referred to as Mg-*x*Al-*y*Ca ht.

The Panalytical Empyrean X-ray diffractometer (XRD) has been utilized with a Cu-$K_{\alpha 1}$ radiation (λ = 1.5406 Å) at 40 kV and 40 mA to conduct a phase identification analysis. A wobble scan (ω = −2, −1, 0, 1, 2°) was used to increase the obtained intensities for the different crystal orientations of the small secondary phases.

The samples for microscopic analysis were grounded using 2000 and 4000 SiC emery papers followed by mechanical polishing using 3 and 1 μm diamond suspension using ethanol as a lubricating agent. Some polished samples have been colour etched with a picric acid-based solution for optical microscopy (grain size analysis). For SEM analysis, the polished samples were subjected to electropolishing using (Streuers) AC 2 electrolyte. Electro-polishing was performed at ≤−20 °C, at 15 V and for 60 s. The waviness arising from electro polishing was later removed by mechanical polishing using colloidal suspension of 0.04 μm SiO_2 particles. The SiO_2 particles were subsequently removed with a rotating polishing cloth and ethanol followed by further cleaning in an ultrasonic bath.

The secondary electron and back scattered electron imaging were performed in the SEM (Helios Nanolab 600i) at an accelerating voltage of 10 kV. The acquired images have been utilized for a digital image analysis of the secondary phase fraction. The threshold was determined with the isodata algorithm according to [35]. EDS measurements in SEM were also performed at an accelerating voltage of 10 kV. EBSD measurements were carried out at an accelerating voltage of 20 kV. Connectivity of the Laves phase was represented in terms of the Euler number and this analysis was performed using the corresponding function in Matlab. The Euler

Table 1
Chemical compositions of the studied alloys analyzed by inductively coupled plasma atomic emission spectroscopy.

Alloy	Al (wt%)	Ca (wt%)	Al (at%)	Ca (at%)	Mg (at%)	Ca/Al (at%/at%)
Mg-6Al-2Ca	5.53	1.74	5.04	1.07	93.89	0.21
Mg-5Al-3Ca	4.65	2.82	4.26	1.74	94.01	0.41
Mg-4Al-4Ca	3.94	3.83	3.62	2.37	94.01	0.65

number is determined by calculating the total number of objects (connected white pixels) in the binary image minus the total number of holes. The smaller and more negative Euler number reflects better connectivity of the Laves phases in Mg-Al-Ca alloys. Since the samples were polished using SiO_2 nanoparticles after electropolishing, to avoid any effect of residual particles on Euler number analysis, the microstructural images were first filtered using the grey scale attribute filtering in Image J. The particles below 10 pixels were removed from the images having dimensions of 1536 × 1024 pixels.

Scanning transmission electron microscopy (STEM) was performed on a Titan Themis microscope (Thermo Fisher Scientific) operated at 300 kV and a Titan G2 ChemiSTEM microscope operated at 200 kV [36]. The probe forming lenses are aberration corrected to enable a convergence angle of 24 mrad and a resulting resolution of 1 Å. Annular bright field (ABF), low angle annular dark field (LAADF), and high angle annular dark field (HAADF) images were collected using detectors with angular ranges 8–16, 17–72, and 73–200 mrad, respectively. The geometric phase analysis was conducted using the code Strain++ developed by J.J.P. Peters, based on the algorithm detailed in the reference [37]. STEM-EDS spectrum imaging was acquired using the SuperX spectrometer, and the dataset was later denoised by multivariate statistical analysis [38]. Quantification of individual phases was based on the Cliff-Lorimer method. Thin lamella samples were prepared on a Scios2 (Thermo Fisher Scientific) focus ion beam (FIB).

Tensile tests were performed on an electromechanical tensile testing machine at room temperature. Dog bone shaped tensile specimen were cut from the as-cast block using spark erosion. For each as-cast or heat-treated alloy, at least three samples were investigated.

Calphad calculations within the Mg-Al-Ca system were performed using Thermo-Calc software [39] with the database from Janz et al. [40]. This database provides the most recent and complete published description of the system.

3. Results

3.1. Phase analysis

The XRD diffractograms of the Mg-Al-Ca alloys in the as-cast and the heat-treated conditions are shown in Fig. 1 a and b respectively. Besides the characteristic Mg reflections, all investigated alloys exhibit additional peaks associated with different Laves phases in the microstructure. The main Laves phases in Mg-6Al-2Ca ac, Mg-5Al-3Ca ac, and Mg-4Al-4Ca ac are C15, C36, and C14, respectively. The lattice parameters of the Laves phases are determined based on the positions of the reflection peaks and listed in Table 2. The indexing of their respective reflections is plotted in Fig. 1 c. Additional peaks corresponding to C36 phases are also present in Mg-6Al-2Ca ac and Mg-4Al-4Ca ac alloys, although they are too minor to reliably define the lattice parameter. After the heat treatment, only the C15 phase is observed in Mg-6Al-2Ca ht and Mg-5Al-3Ca ht, confirming a phase transition from C36 to C15 at elevated temperatures. For Mg-4Al-4Ca ht, C36 and C14 phases still coexist.

3.2. Microstructural analysis

As shown in Fig. 2, the Mg grains in all three alloys are very large. Median grain sizes for Mg-6Al-2Ca, Mg-5Al-3Ca, Mg-4Al-4Ca are 120, 180, and 170 μm, respectively. Moreover, there is no apparent grain growth observed after the performed heat treatment.

In comparison, as shown in Fig. 3, the morphology of the Laves phases changed drastically from interconnected skeletons in the as-cast states to more rounded and dispersed particles after heat treatment. As summarized in Table 2, the increase in Ca/Al ratio results in an increase in area fraction of the Laves phases. For all three alloys, the area fraction of Laves phases also decreases after annealing. For each heat-treated alloy, two images of 0.25 × 0.25 mm^2 area were analysed, which cover a total number of 500–1500 isolated particles. The number density of particles was counted as 7.6, 5.3, and 11.3 × 10^3 mm^{-2} for Mg-6Al-2Ca ht, Mg-5Al-3Ca ht, and Mg-4Al-4Ca ht, respectively, translating to an average spacing of 11.5, 13.7, and 9.4 μm between the particles. Considering the different area fractions of these alloys, the average sizes of their Laves phases are calculated as 2.05, 3.05, and 2.61 μm, respectively, assuming a spherical shape. Due to the anisotropic shape and interconnectivity of the Laves phases in the as-cast microstructure, their number density and size cannot be evaluated in a similar fashion. Instead, the Euler number analysis was applied (556, 42, and −727 for Mg-6Al-2Ca ac, Mg-5Al-3Ca ac, and Mg-4Al-4Ca ac, respectively, where more negative values relate to better interconnectivity [22]) to confirm the visual impression that the interconnectivity increases from Mg-6Al-2Ca ac, Mg-5Al-3Ca ac to Mg-4Al-4Ca ac. As an alternative analysis, longest pathways of the skeleton were evaluated within a field of view of 0.25 × 0.25 mm^2 and determined as 1.1, 3.5, 4.4 mm for Mg-6Al-2Ca ac, Mg-5Al-3Ca ac, and Mg-4Al-4Ca ac, respectively, confirming the same trend of interconnectivity Mg-6Al-2Ca ac < Mg-5Al-3Ca ac < Mg-4Al-4Ca ac.

Chemical compositions of the Laves phases and the Mg matrix were determined for each alloy by EDS. SEM-EDS provides better sampling over many Laves phases [21]. However, the SEM interaction volumes exceed the size of Laves phases and contain signals from the Mg matrix, so that the measurements overestimate Mg concentrations. Therefore, we only rely on STEM-EDS results to determine the chemical formula $Mg_xAl_{2-x}Ca$ of respected Laves phases (Table 2). SEM-EDS mapping was utilized to differentiate the Al-poor Laves phase C14 from the Al-rich Laves phase C36, from which the area fractions of the respective phases in Mg-4Al-4Ca ac and ht alloys are evaluated.

3.3. Orientation relationships between Laves phases and Mg matrix

To observe the OR between Mg and C15/C36/C14, we choose for each case a heat-treated alloy with larger Laves phases to facilitate indexing from EBSD. As shown in Fig. 4, most particles are round in Mg-5Al-3Ca ht, and no particular OR is favoured between Mg and C15. There exists however a small fraction of platelet C15 precipitates, as shown in Fig. 5, where there is a well-defined OR $(0002)_{Mg}//(1\,1\,1)_{C15}$ and $[11\bar{2}0]_{Mg}//[11\bar{2}]_{C15}$. This OR has been reported by Suzuki et al. [24] for small platelet C15 phases in

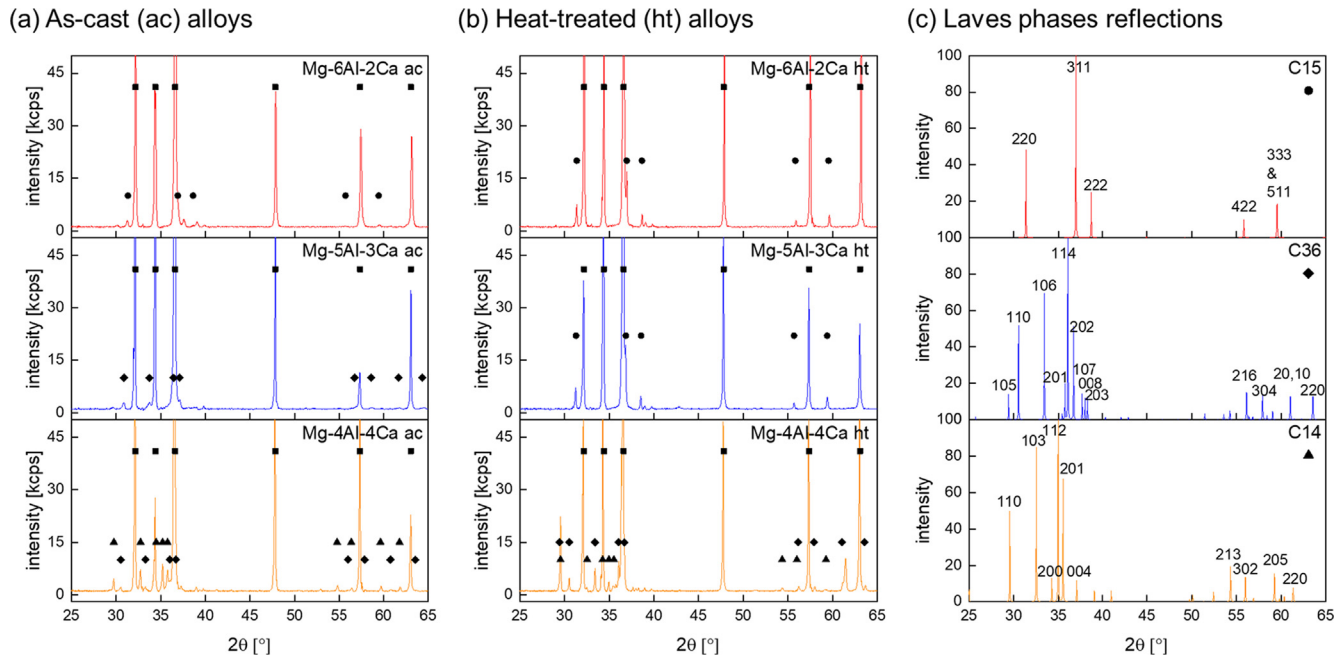

Fig. 1. XRD scans of (a) as-cast (ac) and (b) heat-treated (ht) Mg-6Al-2Ca, Mg-5Al-3Ca, and Mg-4Al-4Ca alloys. Reflections of the Mg, C15, C36, and C14 phases are labelled by squares, circles, diamonds, and triangles, respectively. (c) Indexing of the reflections of C15, C36, and C14 phases.

Table 2
Comparison between the area fraction, lattice parameters, and composition of Laves phases and Mg matrix in different alloys. For compositions determined by STEM-EDS, the fraction x is calculated to fit the chemical formula $Mg_xAl_{2-x}Ca$. For compositions determined in the SEM, x value is not given (denoted by *) to avoid confusion.

Alloy	Phase	Area fraction	a (Å)	c (Å)	Mg at%	Al at%	Ca at%	x
Mg-6Al-2Ca ac	C15	4.2 ± 0.3 % (C15 + C36)	8.07	–	11.5	63.0	25.5	*
	C36		–	–	12.0	56.2	31.9	0.35
	Mg	Bal.	3.21	5.21	96.1	3.8	<0.1	–
Mg-5Al-3Ca ac	C36	7.1 ± 0.5 %	5.79	18.78	15.5	57.5	27.0	0.42
	Mg	Bal.	3.21	5.21	98.8	1.2	<0.1	–
Mg-4Al-4Ca ac	C36	1.3 ± 0.8 %	5.85	19.05	28.9	42.3	28.8	*
	C14	8.3 ± 1.2 %	6.00	9.64	44.7	24.1	31.3	1.30
	Mg	Bal.	3.21	5.22	98.7	1.1	0.2	–
Mg-6Al-2Ca ht	C15	3.2 ± 0.1 %	8.06	–	2.5	67.1	30.5	0.07
	Mg	Bal.	3.21	5.21	97.0	3.0	<0.1	–
Mg-5Al-3Ca ht	C15	4.9 ± 0.5 %	8.08	–	4.6	61.2	34.2	0.14
	Mg	Bal.	3.21	5.22	98.9	1.0	<0.1	–
Mg-4Al-4Ca ht	C36	4.6 ± 0.5 %	5.85	18.94	17.3	50.4	32.3	0.51
	C14	3.1 ± 0.8 %	6.04	9.70	47.3	21.8	30.8	1.34
	Mg	Bal.	3.21	5.23	99.7	0.3	<0.1	–

Mg, and as the precipitates coarsen, the OR is no longer favourable [33].

The atomic arrangement at the Mg/C15 interface was further examined using STEM. As shown in Fig. 5 b–d, the interface is atomically sharp along the Mg basal-plane with the aforementioned OR. Based on the lattice parameters of C15 and Mg phases listed in Table 2, the mismatch between $(1\,1\,1)_{C15}$ and $(0001)_{Mg}$ is −10.5 % with respect to the Mg lattice, and between $(2\bar{2}0)_{C15}$ and $(1\bar{1}00)_{Mg}$, +2.8 %. The short axis along Mg c-axis displays the largest mismatch so that by keeping the platelet shape, the precipitate can have a lower strain energy. To analyse how the smaller mismatch is accommodated in the $(1\,1\,1)_{C15}$ plane, geometric phase analysis was conducted on the interface image in Fig. 5 f. As shown in Fig. 5 g, the out-of-plane direction of C15 is compressively strained with respect to the Mg. The in-plane direction (along the vertical axis), however, shows a matching lattice, and the strain is accommodated by dislocations at the interface (Fig. 5 h). Hence, we confirm the semicoherent interface between the platelet precipitate C15 and the Mg matrix.

The hexagonal Laves phases C36 and C14 were observed in Mg-4Al-4Ca ht. As shown in Fig. 6, there is no apparent OR between these Laves phases and the Mg matrix. Nevertheless, local groups of hexagonal Laves phases with shared OR are observed. Cross-sectional STEM study (Fig. 7) further reveals various interface termination of the hexagonal Laves phase, including but not limited to $(0001)_{C36}$, $(1\bar{1}00)_{C36}$ (Fig. 7 d), $(2\bar{2}01)_{C14}$ (Fig. 7 i). Regardless of the interface, there is a common OR for the C36 phase $(0001)_{C36}$ // $(1\bar{1}01)_{Mg}$ (Fig. 7 d) and for the C14 phase $(0001)_{C14}$// $(1\bar{1}01)_{Mg}$ (Fig. 7 i). The interface plane, $(1\bar{1}00)_{C36}$ or $(2\bar{2}201)_{C14}$, is not parallel to any low index plane of Mg, which is also manifested by the apparent widths of the interfaces (Fig. 7 d,i), caused by a few degrees mistilt off the crystallographic planes. Likewise, there is a few degrees mistilt between the C36/C14 zone axis and the zone axis of the neighbouring Mg grain. Based on the FFT in Fig. 7 e, the neighbouring Mg grain is close to the zone axis $[01\bar{1}1]_{Mg}$, so that there is an approximate OR $[11\bar{2}0]_{C36}$~//$[01\bar{1}1]_{Mg}$. For the C14/Mg interface we observed, the FFT in Fig. 7 j suggests an approximate OR $[11\bar{2}0]_{C14}$~//$[1\bar{1}02]_{Mg}$.

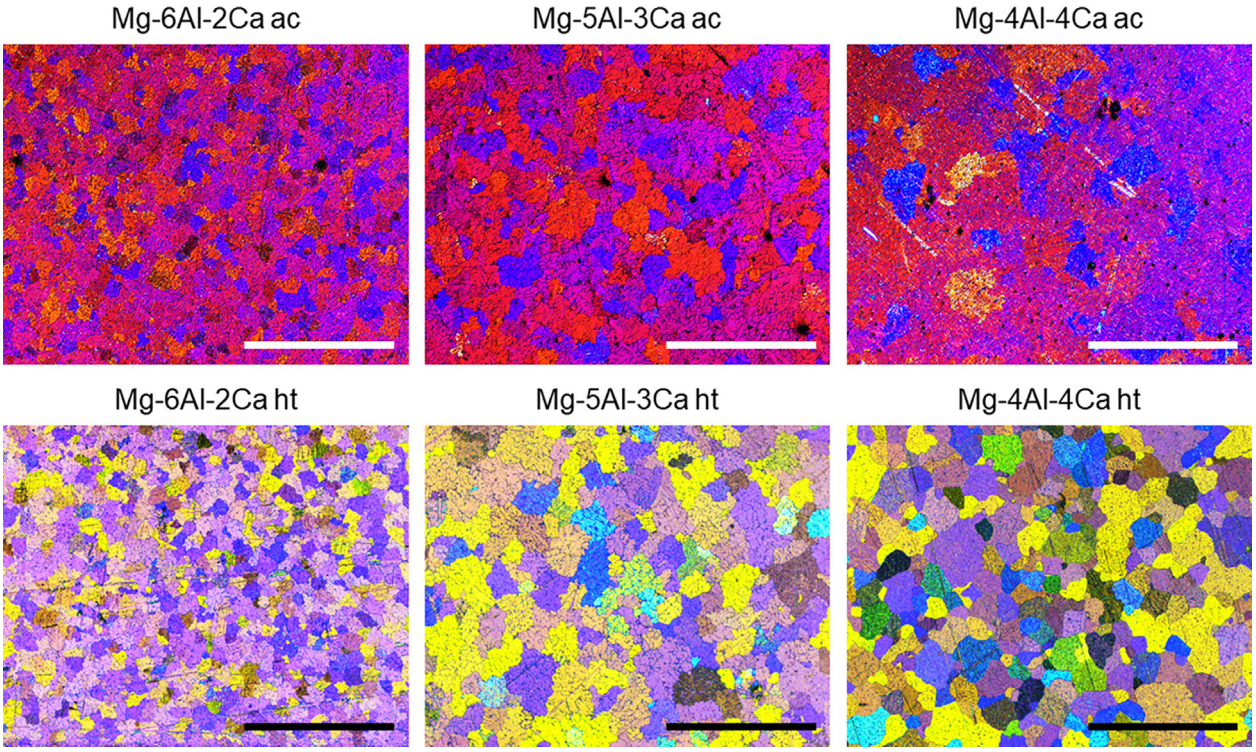

Fig. 2. Etched surfaces of as-cast (ac) and heat-treated (ht) Mg-6Al-2Ca, Mg-5Al-3Ca, and Mg-4Al-4Ca alloys. Scale bars are 1 mm.

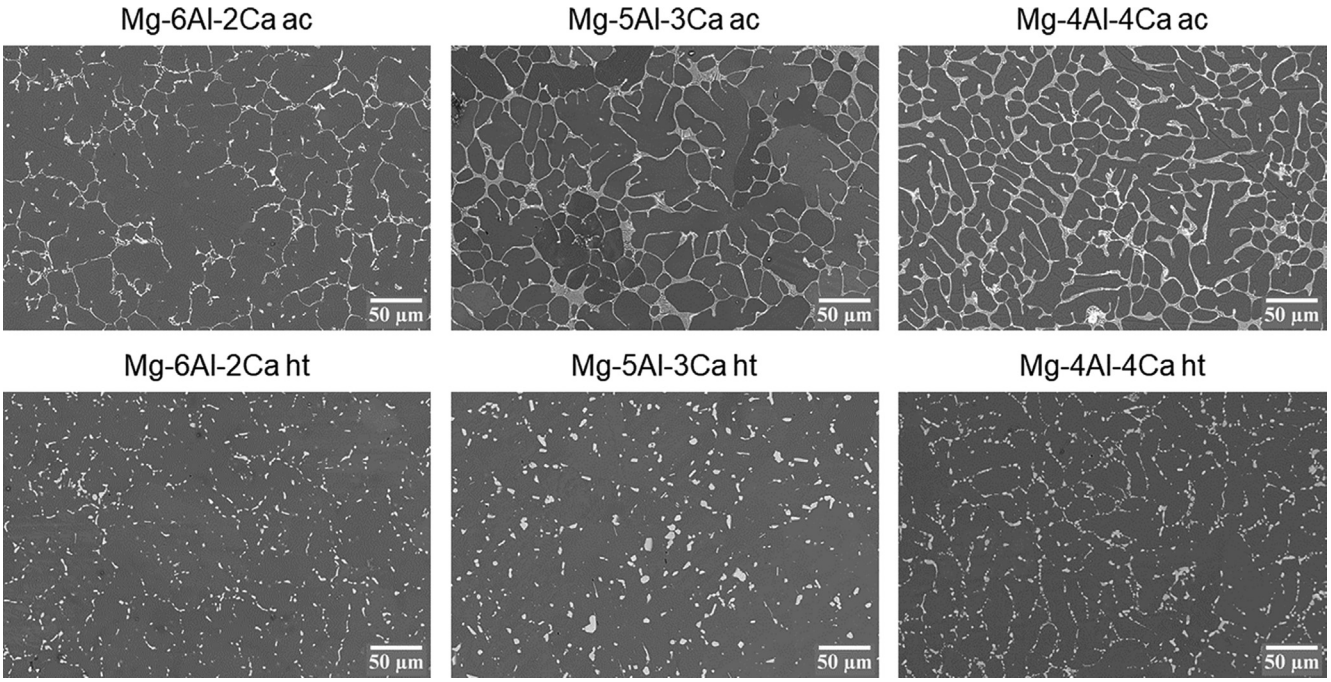

Fig. 3. SEM-backscattered electron images of as-cast (ac) and heat-treated (ht) Mg-6Al-2Ca, Mg-5Al-3Ca and Mg-4Al-4Ca alloys.

The OR $(0001)_{C36\ or\ C14}//(1\bar{1}01)_{Mg}$ can be understood by the minimization of strain energy. $(0004)_{C36}$, $(0002)_{C14}$ and $(1\bar{1}01)_{Mg}$ are all close-packed planes in the respective crystals. Depending on the composition and hence lattice parameters of the C14 and C36 phases (Table 2), the mismatch between $(0008)_{C36}$ or $(0004)_{C14}$ and $(1\bar{1}01)_{Mg}$ planes ranges between −4% and 0 % with respect to the Mg lattice. Due to this small mismatch, the Laves phase could grow to several micrometers in size. The isotropic shape of the particles indicates the mismatch along other dimensions are likely to be small as well, but other ORs we have found involve a few degrees mistilt and are hence only approximate. The OR $(0001)_{C36\ or\ C14}//(1\bar{1}01)_{Mg}$ without specified OR in the second dimension is similar to a fiber texture[45], which is constrained by minimization of strain energy only along one dimension. The resulting interfaces are less coherent than the semi-coherent interface between Mg and the C15 platelet (Fig. 5).

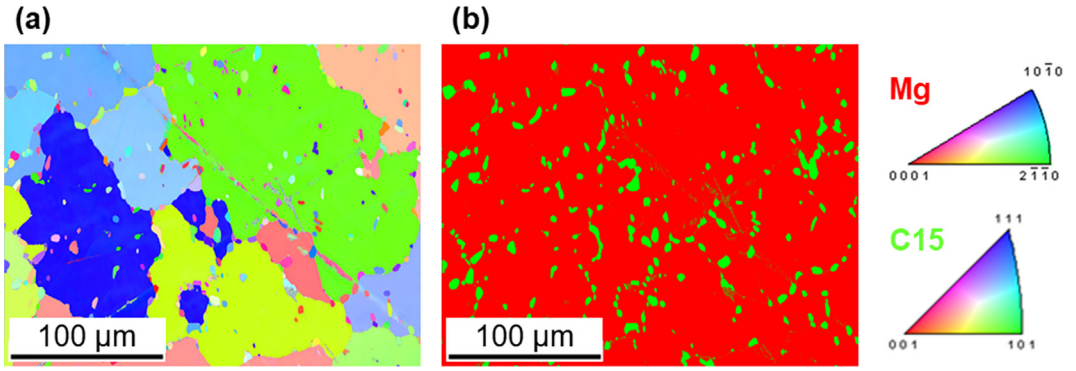

Fig. 4. (a) EBSD-inverse pole figure map and (b) phase map of Mg and C15 phases superimposed on each other for Mg-5Al-3Ca ht.

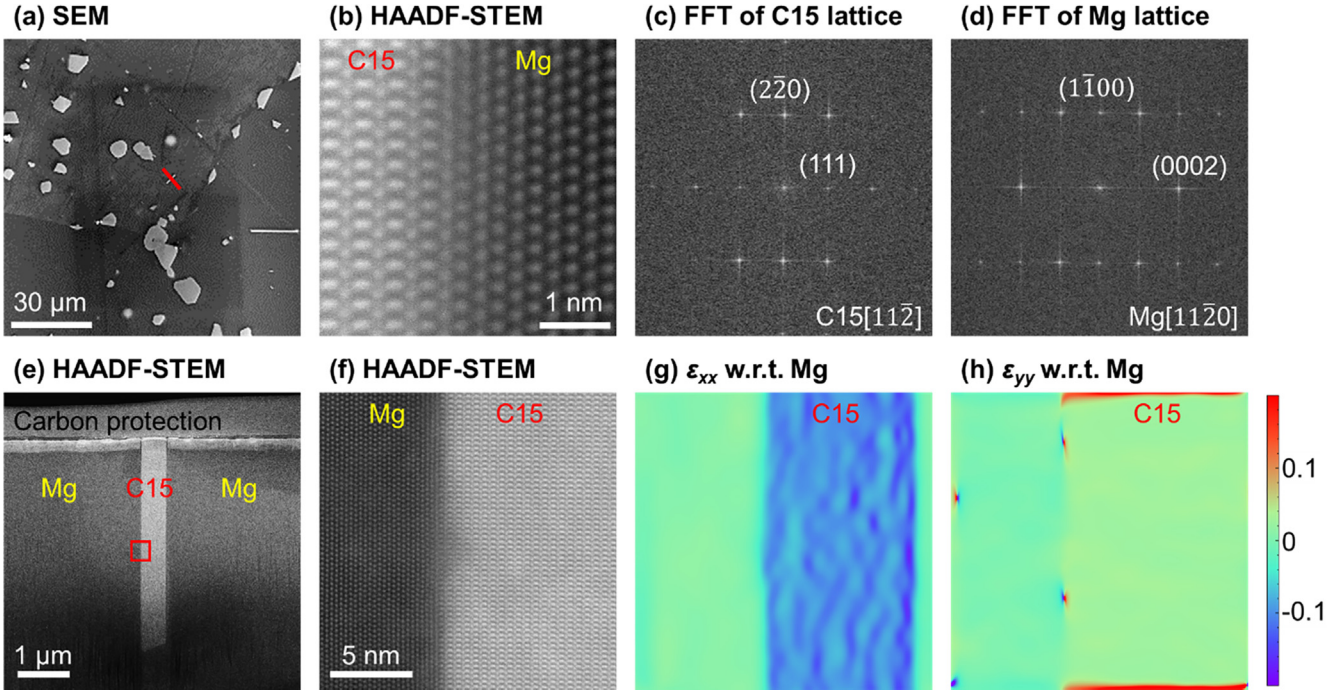

Fig. 5. (a) SEM image of a platelet C15 precipitate highlighted by a red rectangle box, indicating the area for cross-section FIB liftout, (b) the C15/Mg interface at atomic resolution, with the corresponding fast Fourier transform (FFT) on the (c) C15 and (d) Mg lattices to reveal their orientation relationship. (e) Cross-section view of the C15 precipitate within Mg matrix, (f) the left interface between C15 and Mg, with the corresponding geometric phase analysis showing the strain with respect to the Mg matrix along (g) the horizontal and (h) the vertical directions (same color scale). (For interpretation of the references to color in this figure legend, the reader is referred to the web version of this article.)

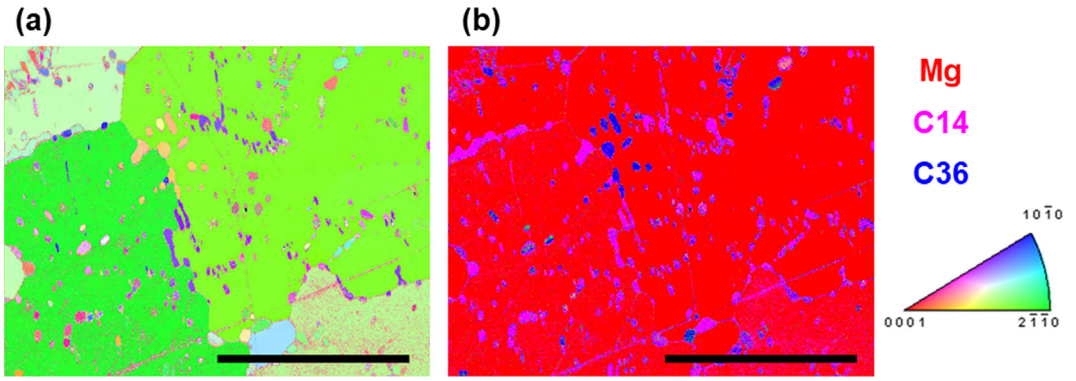

Fig. 6. (a) EBSD-inverse pole figure map and (b) phase map of Mg, C14 and C36 phases superimposed on each other for Mg-4Al-4Ca ht. Scale bars are 100 µm.

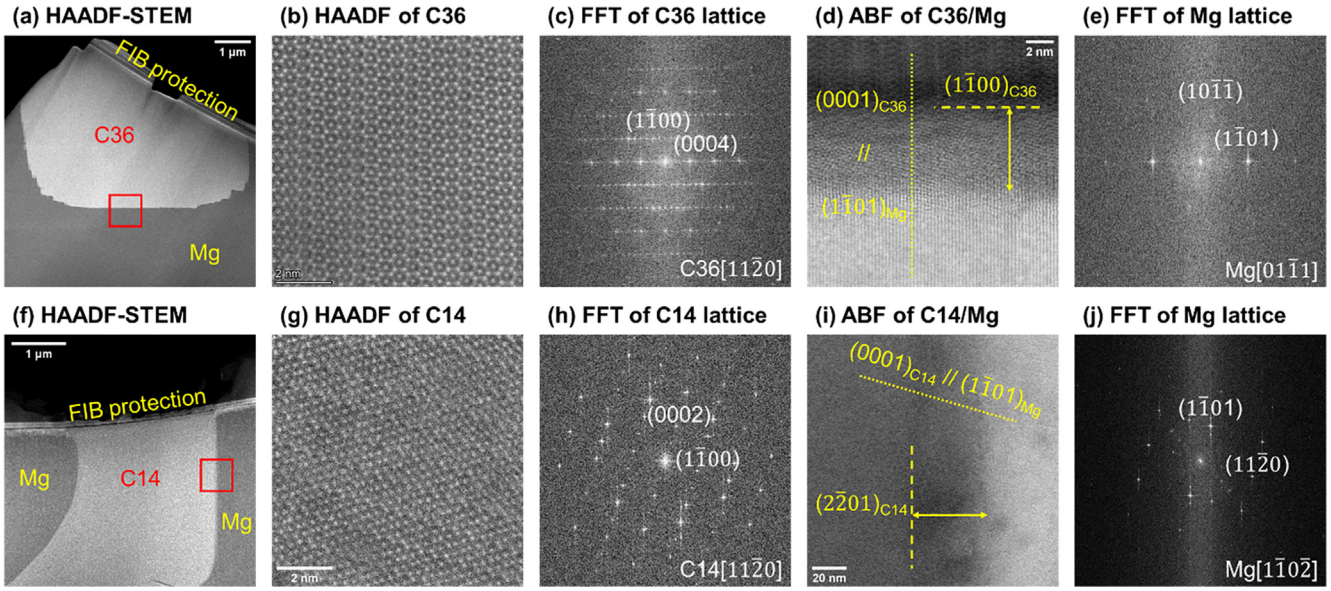

Fig. 7. Analysis of OR between (a–e) a C36 particle, (f–j) a C14 particle and the Mg matrix. (a, f) HAADF-STEM images of the interfaces in cross-section view, (b, g) high resolution HAADF-STEM images of the C36/C14 phases, with (c, h) the corresponding FFT; (d, i) high resolution ABF-STEM images of the interfaces with dotted lines annotating the OR and dashed lines representing the interface planes with a width marked by arrows, indicating mistilt from the interface planes, and (e, j) the corresponding FFT on the Mg lattice to get the approximate OR of the zone axis orientations.

3.4. Mechanical properties of as-cast and heat-treated alloys

As shown in Fig. 8 a and b, for the as-cast alloys the yield strength, $\sigma_{0.2}$, increases with increasing Ca/Al ratio or the amount and connectivity of Laves phases. Moreover, uniform elongation reduces with an increase in Ca/Al ratio (Fig. 8 c) because during tensile loading, cracks tend to nucleate and grow in the Laves phase [16,21,22]. The ultimate tensile strength (UTS) does not vary with Ca/Al ratio (Fig. 8 d), which is attributed to the inverse relationship between the yield strength and uniform elongation. The mechanical properties changed significantly once the alloys were heat-treated at 500 °C (Fig. 8 a–d). Both UTS and uniform elongation improved considerably at the expense of the yield strength.

4. Modelling and discussion

4.1. Calphad modelling

Firstly, we apply thermodynamic modelling using the database from Janz et al. [40] to discuss the microstructure observed in the heat-treated alloys. As shown in the calculated isothermal sections of the Mg-Al-Ca system at 500 °C (Fig. 9 a) and 400 °C (Fig. 9 b), the C36 phase region shrinks with decreasing temperature, whereas the C15 phase region expands. According to the experimental phase diagram study by Suzuki et al. [27], the C36 phase is located between the C14 and C15 phases. Hence, the calculated location of the C36 phase at 500 °C (Fig. 9 a) is likely inaccurate. Nevertheless, for the Mg-rich corner, there is a good agreement between the modelled diagrams (Fig. 9 a and b) and the phase analysis performed at the respective temperatures by Suzuki et al. [27]: The (Mg) phase is in equilibrium with the C14 and C36 Laves phases at 500 °C, but not with C15. At 400 °C, (Mg) is in equilibrium with the C14 and C15 Laves phases.

A close-up of the Mg-rich corner is shown in Fig. 9 c (500 °C) and Fig. 9 d (400 °C), including the three investigated heat-treated alloys. For alloys equilibrated at 500 °C, Mg-6Al-2Ca and Mg-5Al-3Ca are expected to contain C36 in the (Mg) matrix, and Mg-4Al-4Ca is expected to contain both C14 and C36. Nevertheless, the heat-treated alloys in this study, Mg-6Al-2Ca ht and Mg-5Al-3Ca ht, have C15 Laves phases instead of C36. During annealing at 500 °C, it can be assumed that an equilibrium state was reached after 48 h. Although the experimental furnace cooling does not directly correspond to an equilibrium at any specific temperature, it is worth exploring phase equilibria at lower temperatures to understand the effect of cooling. By comparing Fig. 9 c and d, it is apparent that the stability range of C36 shrinks as the temperature decreases. For the three alloy compositions, the transition temperatures of C36 to C15 are evaluated as 490 °C (Mg-6Al-2Ca), 470 °C (Mg-5Al-3Ca), and 390 °C (Mg-4Al-4Ca). Particularly for Mg-6Al-2Ca and Mg-5Al-3Ca, a mild decrease in temperature would drive the C36 to C15 transition, and we hence attribute the slow furnace cooling after the 500 °C annealing to the observed C15 phases in both alloys. The calculated molar/volume fractions and the chemical compositions of the Laves phases are summarized in Table 3, for equilibria at 400 °C and 500 °C. Coincidentally, the experimentally observed phase fractions and compositions of the heat-treated alloys (Table 2) are close to the modelled results at 400 °C. Nevertheless, the good match with the calculation at 400 °C suggests that further phase transformation and partitioning below 400 °C was kinetically hindered.

4.2. Microstructural analysis

As shown in Table 1, the total atomic contents of alloying elements are roughly the same in all the studied alloys. However, the Mg matrix dissolves an appreciable amount of Al, but not Ca (Table 2), so that the alloys containing more Ca have higher fractions of Laves phases. After annealing, the calculated fractions of the intermetallic phases (Table 3) are very similar to the experimentally observed fractions. The measured fractions in the as-cast alloys are higher than after annealing. According to Table 2, after annealing, C36 phases in Mg-6Al-2Ca and Mg-5Al-3Ca alloys are transformed to C15, while some C14 phase in Mg-4Al-4Ca is transformed to C36. Although the overall stability of C36 decreases as the alloys cool down from 500 to 400 °C (narrower ranges of C36 in Fig. 9 d than Fig. 9 c), we note that Mg-4Al-4Ca stays in the (Mg) + C14 + C36 phase field and becomes closer to the

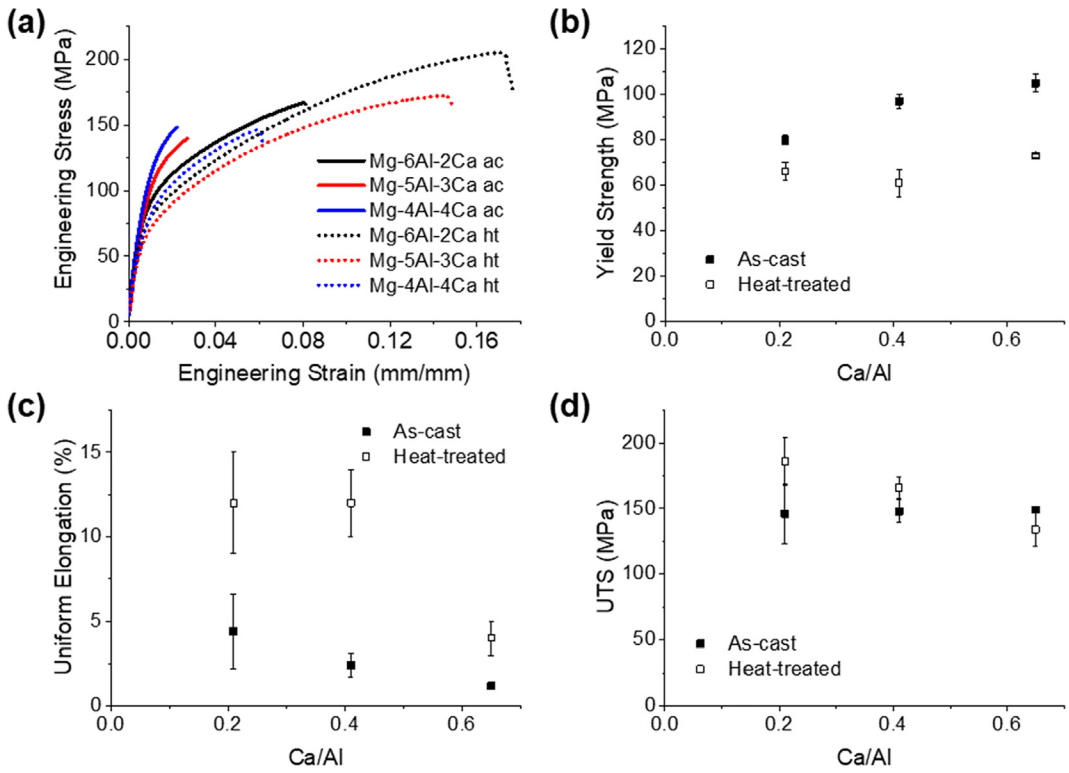

Fig. 8. (a) engineering stress–strain curves for as-cast and heat-treated alloys tested at room temperature. Tensile properties of Mg-Al-Ca alloys in as-cast and heat-treated state: (b) yield strength, (c) uniform elongation, and (d) ultimate tensile strength (UTS) for all alloys under study.

(Mg) + C36 border as the temperature decreases. This can explain the increase of the C36 phase fraction in Mg-4Al-4Ca after annealing and furnace cooling. In both cases, the phases after transformation have higher contents in alloying elements (C15 > C36 > C14), so that their phase fractions are consequently reduced.

As shown in Table 2, the lattice parameters of the Laves phase $Mg_xAl_{2-x}Ca$ are correlated to their chemical composition, becoming larger with increasing x. For C15, we observed the highest Mg content in Mg-5Al-3Ca ht, close to $Mg_{0.14}Al_{1.86}Ca$, leading to a = 8.08 Å, which is ~0.5 % larger than Al_2Ca (x = 0). For C36, a big composition range of $Mg_xAl_{2-x}Ca$, $0.66 \leq x \leq 1.07$, was observed in bulk intermetallics [29]. The present results extend the lower range to x = 0.51 in the heat-treated alloy Mg-4Al-4Ca ht and further down to x = 0.35–0.42 in the as-cast alloys Mg-6Al-2Ca ac and Mg-5Al-3Ca ac. The C14 phase has been reported to exhibit a chemical composition in the range $1.56 \leq x \leq 2$ [29]. The presented experimental results extend the lower range to x = 1.37 in the heat-treated alloy Mg-4Al-4Ca ht and further down to x = 1.30 in the as-cast alloy Mg-4Al-4Ca ac.

4.3. Mechanical properties

We firstly compare the mechanical properties between the as-cast and heat-treated alloys. After annealing, their yield strength decreases, whereas the uniform elongation and UTS improve. This can be attributed to the reduction in area fraction of intermetallic phases after heat treatment in all three alloys (Table 2). Moreover, the breakage of interconnected skeleton (Fig. 3) also plays a major role, as discontinuous particles cannot block dislocation motion as effectively as a continuous intermetallic skeleton [3,4].

To understand the trend of three as-cast alloys, with yield strength Mg-4Al-4Ca ac > Mg-5Al-3Ca ac > Mg-6Al-2Ca ac, we examine the following three factors: Firstly, the grain size (Hall-Petch) strengthening cannot be the dominant factor, as Mg-6Al-2Ca ac has the smallest grain size but lowest yield strength. Secondly, the yield strength correlates well to the area fraction of the Laves phase (Table 2). Last but not least, we note that the yield strength also correlates to the connectivity of the Laves phase as characterized by the Euler number. This is in line with the earlier work on Mg-Al-Ca alloys [21]. The interconnected skeleton carries load more effectively as compared to the loosely connected Laves phase skeleton [4]. Therefore, $\sigma_{0.2}$ values are systematically higher for the as-cast materials than their heat-treated counterparts and within as-cast materials, Mg-4Al-4Ca and Mg-5Al-3Ca alloys (possessing well connected Laves phase skeletons) exhibit $\sigma_{0.2}$ values higher than Mg-6Al-2Ca alloy with Laves phase skeleton of significantly weaker connectivity (with 3 to 4 times shorter connectivity pathways).

Likewise, we examine the same three factors for the trend of heat-treated alloys, with yield strength Mg-4Al-4Ca ht > Mg-6Al-2Ca ht > Mg-5Al-3Ca ht. Grain size strengthening is again excluded as the major factor, as discussed above for as-cast alloys. Moreover, the yield stress behaviour does not directly correlate with the volume fraction of Laves phase, as Mg-6Al-2Ca ht containing 3.2 % of C15 phase has higher yield strength than Mg-5Al-3Ca ht with 4.9 % of C15 phase, which contradicts the rule of mixtures. This is expected, as with the breakdown of the interconnected skeleton during heat treatment, the load is no longer shared effectively between matrix and reinforcement, giving an isostress rather than isostrain condition. Nonetheless, the number density of particles follows the same trend as their yield strength. Indeed fine size and large density of particles are known to be effective in blocking dislocations movements [41]. Therefore, for as-cast and heat-treated alloys, the interconnectivity and dispersion of Laves phases are the respective deciding factors for a high yield stress.

For the Orowan mechanism to operate, the strengthening particles need to resist being cut by dislocation slip from the matrix. Indeed, well-defined OR between Mg and the Laves phases was

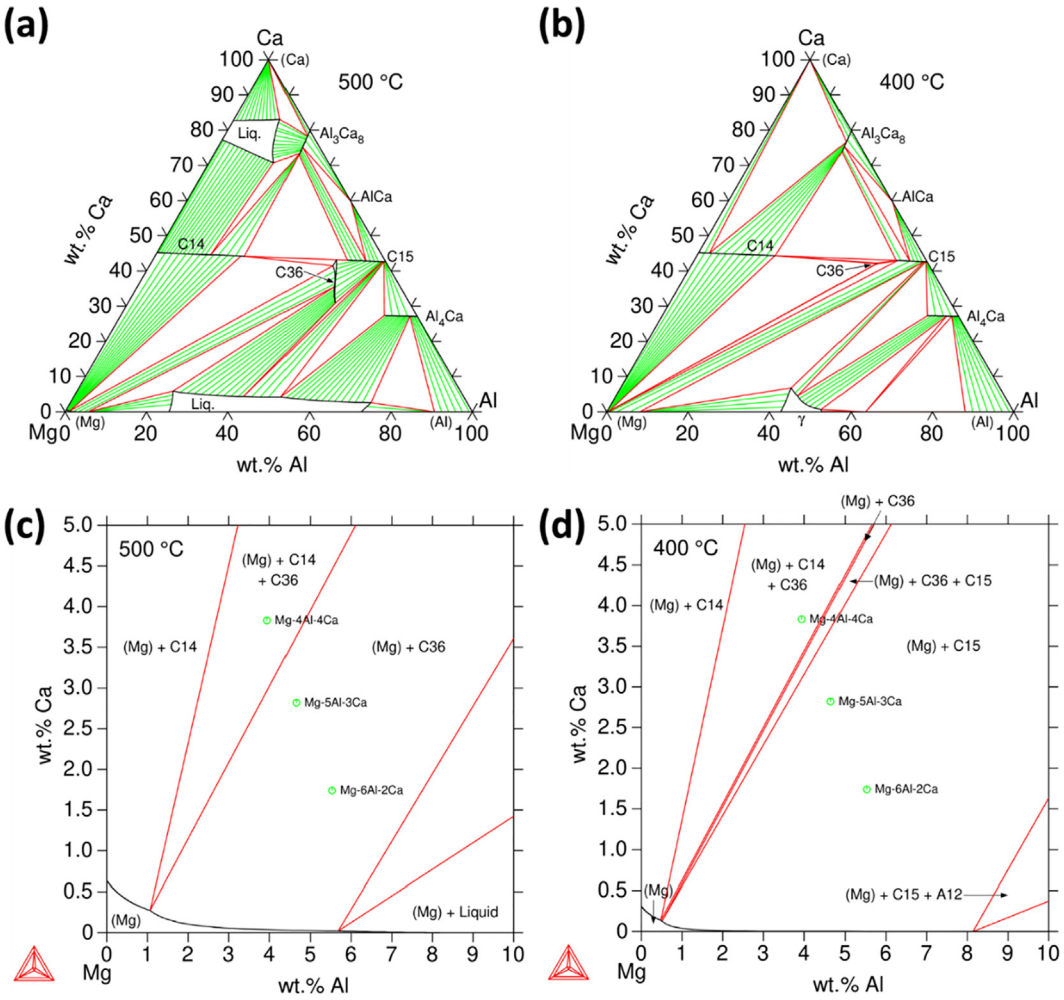

Fig. 9. Thermodynamic calculations in the Mg-Al-Ca system using the database from Janz et al. [40]. Isothermal sections at (a) 500 °C and (b) 400 °C, and close-up views at the respective isothermal sections at (c) 500 °C and (d) 400 °C for the Mg-rich corner showing the location of the three investigated alloys.

Table 3
Calculated compositions and volume fractions of the phases in the modelled alloys equilibrated at 500 °C and 400 °C. The cell volumes derived from the XRD analysis (Table 2) were applied to convert molar fraction into volume fraction.

Alloy	Phase	Mol. fraction	Vol. fraction	Mg at%	Al at%	Ca at%
Mg-6Al-2Ca	C36	3.7 %	3.7 %	18.5	53.1	28.4
500 °C	Mg	Bal.	Bal.	96.8	3.2	0.02
Mg-5Al-3Ca	C36	5.4 %	5.4 %	17.2	52.0	30.8
500 °C	Mg	Bal.	Bal.	98.5	1.4	0.08
Mg-4Al-4Ca	C36	4.0 %	4.0 %	17.1	51.2	31.8
500 °C	C14	2.8 %	3.1 %	43.0	23.6	33.3
	Mg	Bal.	Bal.	98.9	0.95	0.15
Mg-6Al-2Ca	C15	3.2 %	3.0 %	1.8	64.9	33.3
400 °C	Mg	Bal.	Bal.	96.9	3.1	0.002
Mg-5Al-3Ca	C15	5.2 %	4.9 %	4.3	62.4	33.3
400 °C	Mg	Bal.	Bal.	98.9	1.1	0.02
Mg-4Al-4Ca	C36	5.7 %	5.7 %	16.2	51.5	32.3
400 °C	C14	1.4 %	1.6 %	45.3	21.5	33.3
	Mg	Bal.	Bal.	99.5	0.4	0.08

rarely found in the studied alloys. For C36 and C14, we have only found an OR with Laves phase *c*-plane parallel to Mg(1$\bar{1}$01). Without a direct relation to the Mg *c*-plane, the interface with hexagonal Laves phases would be able to block basal slip transfer from Mg. Although the observed semi-coherent interface of C15 Laves phase is parallel to the Mg *c*-plane, the large lattice mismatch perpendicular to the interface inhibits the growth of the platelet precipitates, making them the minority microstructure.

In addition to the onset of plasticity, represented by the yield strength, the properties associated with continuing deformation beyond the elastic limit, UTS and uniform elongation, are also considerably affected by the microstructure. Depending on the material's application, an individual or combination of these properties is most important. Often, the aim is a good compromise between UTS and elongation to achieve high strength while avoiding sudden brittle failure. As an estimate of this property combina-

tion, we examine the product of UTS and uniform elongation (MPa %) [42,43] in Fig. 10.

All as-cast alloys achieve comparatively poorer trade-offs between UTS and uniform elongation. However, their use-case in application would normally be associated much more strongly with the yield strength, as these alloys are typically investigated for long-term creep strength. Previous work has shown that under these conditions, high temperature and low stresses compared to the UTS, the skeleton is particularly effective in strengthening the material [4,21].

The heat-treated alloys exhibit a better balance of strength and ductility compared with their as-cast counterparts. Mg-6Al-2Ca ht (Ca/Al = 0.21 in Fig. 10), which consists of Mg matrix reinforced with a higher number density of C15 particles than Mg-5Al-3Ca ht (Ca/Al = 0.41), exhibits the best product of UTS and uniform elongation among all. While C15, C14, and C36 Laves phases have all been shown to exhibit some plasticity [6,30–34], Mg-4Al-4Ca ht with C36 and C14 particles as strengthening phase has the worst strength-ductility balance among the heat-treated alloys (Fig. 10). Cubic C15 Laves phases are generally thought to deform by dislocation slip on the {111}<1$\bar{1}$0> systems [33,34,44], giving many more slip planes to accommodate deformation than basal slip in the hexagonal C14 or C36 [6,30]. Zhu et al. [33] have found that a Mg-6Al-1Ca alloy under tensile loading exhibited considerable ductility and high work hardening capabilities. They attributed high ductility and work hardening characteristics of the alloy to the presence of deformable C15 Laves phase within the Mg matrix. Moreover, the OR and semi-coherency between Mg (0 0 0 1) and C15 (1 1 1) may enable slip transfer across the particle interface. On the other hand, the incoherent interfaces between Mg and C14/C36 may hinder the basal slip transfer and further contribute to the lack of strength-ductility balance.

Overall, this work reveals new avenues for research to achieve tailored combinations of yield strength, UTS, and elongation to failure by elucidating the balance between interfaces suitable for dislocation transmission and intrinsic strength of the reinforcing phase. Whether an intermediate microstructure based on the C15 phase but with effective load sharing in a skeleton-like reinforcement can be realised and would lead to improved properties will depend on the relative energies of dominant interfaces governing microstructure evolution and the achieved transmission of dislocations through Mg/C15 interfaces. These in turn are controlled by the atomic structure of the interfaces and the relative critical resolved shear stresses on the active slip systems in co-deformation, both of which will require further experimental and computational study.

5. Conclusions

This study investigates different Laves phases in Mg-Al-Ca alloys and their evolution after annealing at 500 °C and furnace cooling. The following conclusions are drawn regarding their crystal structure, microstructure, interfaces, and mechanical properties.

- The annealed Mg-6Al-2Ca and Mg-5Al-3Ca alloys have C15 Laves phases, and a combination of C36 and C14 phases are found in Mg-4Al-4Ca ht. The observed Laves phase fractions and compositions can be compared with equilibrium Calphad calculations. In the as-cast states, the alloys have higher fractions of Laves phases, as those phases are richer in Mg (C36 in Mg-6Al-2Ca and Mg-5Al-3Ca, more C14 than C36 in Mg-4Al-4Ca ac).

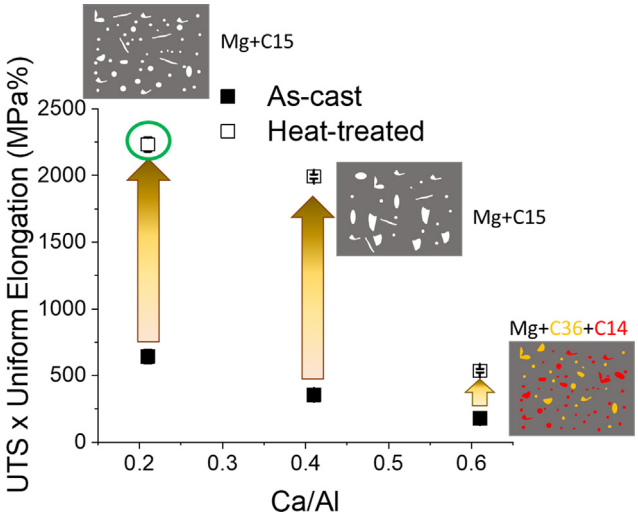

Fig. 10. Strength-ductility balance as the product of UTS and uniform elongation for as-cast and heat-treated Mg-Al-Ca alloys over the Ca/Al ratio. The alloy demonstrating the best balance between strength and ductility is highlighted using a green circle. (For interpretation of the references to color in this figure legend, the reader is referred to the web version of this article.)

- The interconnectivity of the Laves phases increases with Ca/Al ratio for the as-cast alloys. After annealing, the interconnected skeleton was transformed to finely dispersed and more rounded particles.
- The platelets of C15 Laves phase in the heat treated state exhibit an OR with the Mg matrix such that $(0001)_{Mg}//(1\,1\,1)_{C15}$ and $[11\bar{2}0]_{Mg}//[11\bar{2}]_{C15}$. However, this OR is lost when C15 grains grow and approach a spherical shape. Furthermore, in several cases, C36 and C14 particles exhibit a parallel *c*-plane to $(1\bar{1}01)_{Mg}$, but less defined OR along the second dimension, leading to less coherent interfaces.
- After annealing, the yield strengths of all alloys decreased, while their uniform elongation improved, as well as the UTS of two studied alloys. The yield strength of as-cast alloys is related to the volume fraction of the Laves phases as well as their interconnectivity. On the other hand, the yield strength of heat-treated alloys is related to the number density of the dispersed particles. The alloys with C15 particles as strengthening phase show the best strength-ductility balance.

Data availability

Data will be made available on request.

Declaration of Competing Interest

The authors declare that they have no known competing financial interests or personal relationships that could have appeared to influence the work reported in this paper.

Acknowledgements

We thank René D. Pütz for his technical supports. This work was supported by the German research foundation (DFG) within the Collaborative Research Centre SFB 1394 “Structural and Chemical Atomic Complexity—From Defect Phase Diagrams to Materials Properties” (Project ID 409476157) including the project groups A03, A04, B01, C02, C03, C04, C06. H.S. wishes to acknowledge financial support through the Heisenbergprogram of the DFG (SP 1666/2-1). R.B.V. acknowledges the support from the International

Max Planck Research School for Interface Controlled Materials for Energy Conversion (IMPRS-SurMat).

References

[1] B.R. Powell, P.E. Krajewski, A.A. Luo, Chapter 4 - Magnesium alloys for lightweight powertrains and automotive structures, in: P.K. Mallick (Ed.), Materials, Woodhead Publishing, Design and Manufacturing for Lightweight Vehicles, 2021, pp. 125–186.

[2] B. Kondori, R. Mahmudi, Effect of Ca additions on the microstructure, thermal stability and mechanical properties of a cast AM60 magnesium alloy, Mater. Sci. Eng. A 527 (7) (2010) 2014–2021.

[3] D. Amberger, P. Eisenlohr, M. Göken, Microstructural evolution during creep of Ca-containing AZ91, Mater. Sci. Eng. A 510–511 (2009) 398–402.

[4] D. Amberger, P. Eisenlohr, M. Goken, On the importance of a connected hard-phase skeleton for the creep resistance of Mg alloys, Acta Mater. 60 (5) (2012) 2277–2289.

[5] Y. Nakaura, A. Watanabe, K. Ohori, Effects of Ca,Sr additions on properties of Mg-Al based alloys, Mater. Trans. 47 (4) (2006) 1031–1039.

[6] M. Zubair, S. Sandlöbes-Haut, M. Lipińska-Chwałek, M.A. Wollenweber, C. Zehnder, J. Mayer, J.S.K.L. Gibson, S. Korte-Kerzel, Co-deformation between the metallic matrix and intermetallic phases in a creep-resistant Mg-3.68Al-3.8Ca alloy, Mater. Des. 210 (2021) 110113.

[7] J.-F. Nie, Precipitation and hardening in magnesium alloys, Metall. Mater. Trans. A 43 (11) (2012) 3891–3939.

[8] D. Andre, M. Freund, U. Rehman, W. Delis, M. Felten, J. Nowak, C. Tian, M. Zubair, L. Tanure, L. Abdellaoui, H. Springer, J.P. Best, D. Zander, G. Dehm, S. Sandlöbes-Haut, S. Korte-Kerzel, Metallographic preparation methods for the Mg based system Mg-Al-Ca and its Laves phases, Mater Charact 192 (2022) 112187.

[9] F. Stein, A. Leineweber, Laves phases: a review of their functional and structural applications and an improved fundamental understanding of stability and properties, J. Mater. Sci. 56 (9) (2020) 5321–5427.

[10] Y. Xue, N. Takata, H. Li, M. Kobashi, L. Yuan, Critical resolved shear stress of activated slips measured by micropillar compression tests for single-crystals of Cr-based Laves phases, Mater. Sci. Eng. A 806 (2021) 140861.

[11] C.D. Rabadia, Y.J. Liu, L.Y. Chen, S.F. Jawed, L.Q. Wang, H. Sun, L.C. Zhang, Deformation and strength characteristics of Laves phases in titanium alloys, Mater. Des. 179 (2019) 107891.

[12] Y. Yang, Q. Lei, H. Liu, J. Hong, Z. Han, Q. An, J. Shan, X. Chen, H. Xu, Z. Xiao, S. Gong, Cr-based second phases in a high conductivity Cu-Cr-Nb alloy with high high-temperature strength, Mater. Des. 219 (2022) 110784.

[13] W. Luo, C. Kirchlechner, J. Zavašnik, W. Lu, G. Dehm, F. Stein, Crystal structure and composition dependence of mechanical properties of single-crystalline $NbCo_2$ Laves phase, Acta Mater. 184 (2020) 151–163.

[14] R.L. Johnston, R. Hoffmann, The kagome net - band theoretical and topological aspects, Polyhedron 9 (15–16) (1990) 1901–1911.

[15] K.S. Kumar, P.M. Hazzledine, Polytypic transformations in Laves phases, Intermetallics 12 (7–9) (2004) 763–770.

[16] S. Sanyal, M. Paliwal, T.K. Bandyopadhyay, S. Mandal, Evolution of microstructure, phases and mechanical properties in lean as-cast Mg–Al–Ca–Mn alloys under the influence of a wide range of Ca/Al ratio, Mater. Sci. Eng. A 800 (2021) 140322.

[17] B. Kondori, R. Mahmudi, Effect of Ca additions on the microstructure and creep properties of a cast Mg–Al–Mn magnesium alloy, Mater. Sci. Eng. A 700 (2017) 438–447.

[18] Z.T. Li, X.D. Zhang, M.Y. Zheng, X.G. Qiao, K. Wu, C. Xu, S. Kamado, Effect of Ca/Al ratio on microstructure and mechanical properties of Mg-Al-Ca-Mn alloys, Mater. Sci. Eng. A 682 (2017) 423–432.

[19] L. Zhang, K.-K. Deng, K.-B. Nie, F.-J. Xu, K. Su, W. Liang, Microstructures and mechanical properties of Mg–Al–Ca alloys affected by Ca/Al ratio, Mater. Sci. Eng. A 636 (2015) 279–288.

[20] S.M. Liang, R.S. Chen, J.J. Blandin, M. Suery, E.H. Han, Thermal analysis and solidification pathways of Mg–Al–Ca system alloys, Mater. Sci. Eng. A 480 (1) (2008) 365–372.

[21] M. Zubair, S. Sandlöbes, M.A. Wollenweber, C.F. Kusche, W. Hildebrandt, C. Broeckmann, S. Korte-Kerzel, On the role of Laves phases on the mechanical properties of Mg-Al-Ca alloys, Mater. Sci. Eng. A 756 (2019) 272–283.

[22] M. Zubair, S. Sandlöbes-Haut, M.A. Wollenweber, K. Bugelnig, C.F. Kusche, G. Requena, S. Korte-Kerzel, Strain heterogeneity and micro-damage nucleation under tensile stresses in an Mg–5Al–3Ca alloy with an intermetallic skeleton, Mater. Sci. Eng. A 767 (2019).

[23] A.A. Luo, B.R. Powell, M.P. Balogh, Creep and microstructure of magnesium-aluminum-calcium based alloys, Metall. Mater. Trans. A 33 (3) (2002) 567–574.

[24] A. Suzuki, N.D. Saddock, J.R. TerBush, B.R. Powell, J.W. Jones, T.M. Pollock, Precipitation strengthening of a Mg-Al-Ca–based AXJ530 die-cast alloy, Metall. Mater. Trans. A 39 (3) (2008) 696–702.

[25] N.D. Saddock, A. Suzuki, J.W. Jones, T.M. Pollock, Grain-scale creep processes in Mg–Al–Ca base alloys: implications for alloy design, Scr. Mater. 63 (7) (2010) 692–697.

[26] A. Suzuki, N.D. Saddock, J.W. Jones, T.M. Pollock, Solidification paths and eutectic intermetallic phases in Mg–Al–Ca ternary alloys, Acta Mater. 53 (9) (2005) 2823–2834.

[27] A. Suzuki, N.D. Saddock, J.W. Jones, T.M. Pollock, Phase equilibria in the Mg-Al-Ca ternary system at 773 and 673 K, Metall. Mater. Trans. A 37 (3) (2006) 975–983.

[28] K. Söderberg, Y. Kubota, N. Muroyama, D. Grüner, A. Yoshimura, O. Terasaki, Electron charge distribution of $CaAl_{2-x}Zn_x$: Maximum entropy method combined with Rietveld analysis of high-resolution-synchrotron X-ray powder diffraction data, J. Solid State Chem. 181 (8) (2008) 1998–2005.

[29] S. Amerioun, S.I. Simak, U. Häussermann, Laves-phase structural changes in the system $CaAl_{2-x}Mg_x$, Inorg. Chem. 42 (5) (2003) 1467–1474.

[30] J. Guénolé, M. Zubair, S. Roy, Z. Xie, M. Lipińska-Chwałek, S. Sandlöbes-Haut, S. Korte-Kerzel, Exploring the transfer of plasticity across Laves phase interfaces in a dual phase magnesium alloy, Mater. Des. 109572 (2021).

[31] M. Freund, D. Andre, C. Zehnder, H. Rempel, D. Gerber, M. Zubair, S. Sandlöbes-Haut, J.S.K.L. Gibson, S. Korte-Kerzel, Plastic deformation of the $CaMg_2$ C14-Laves phase from 50–250 °C, Materialia 20 (2021) 101237.

[32] C. Zehnder, K. Czerwinski, K.D. Molodov, S. Sandlöbes-Haut, J.S.K.L. Gibson, S. Korte-Kerzel, Plastic deformation of single crystalline C14 Mg_2Ca Laves phase at room temperature, Mater. Sci. Eng. A 759 (2019) 754–761.

[33] G. Zhu, L. Wang, J. Wang, J. Wang, J.-S. Park, X. Zeng, Highly deformable Mg–Al–Ca alloy with Al_2Ca precipitates, Acta Mater. 200 (2020) 236–245.

[34] S. Luo, L. Wang, J. Wang, G. Zhu, X. Zeng, Micro-compression of Al_2Ca particles in a Mg-Al-Ca alloy, Materialia (2021) 101300.

[35] Mathematical Image Processing (2018).

[36] A. Kovács, R. Schierholz, K. Tillmann, FEI Titan G2 80–200 CREWLEY, J. Large-Scale Res. Facil. JLSRF 2 (A43) (2016).

[37] M.J. Hÿtch, E. Snoeck, R. Kilaas, Quantitative measurement of displacement and strain fields from HREM micrographs, Ultramicroscopy 74 (3) (1998) 131–146.

[38] S. Zhang, C. Scheu, Evaluation of EELS spectrum imaging data by spectral components and factors from multivariate analysis, Microscopy 67 (suppl_1) (2018) i133–i141.

[39] J.O. Andersson, T. Helander, L. Höglund, P. Shi, B. Sundman, Thermo-Calc & DICTRA, computational tools for materials science, Calphad 26 (2) (2002) 273–312.

[40] A. Janz, J. Gröbner, H. Cao, J. Zhu, Y.A. Chang, R. Schmid-Fetzer, Thermodynamic modeling of the Mg–Al–Ca system, Acta Mater. 57 (3) (2009) 682–694.

[41] R.E. Smallman, A.H.W. Ngan, Chapter 13 - precipitation hardening, in: R.E. Smallman, A.H.W. Ngan (Eds.), Modern Physical Metallurgy (Eighth Edition), Butterworth-Heinemann, Oxford, 2014, pp. 499–527.

[42] Y. Ogawa, H. Hosoi, K. Tsuzaki, T. Redarce, O. Takakuwa, H. Matsunaga, Hydrogen, as an alloying element, enables a greater strength-ductility balance in an Fe-Cr-Ni-based, stable austenitic stainless steel, Acta Mater. 199 (2020) 181–192.

[43] M. Koyama, T. Sawaguchi, K. Tsuzaki, TWIP effect and plastic instability condition in an Fe-Mn-C austenitic steel, ISIJ Int. 53 (2) (2013) 323–329.

[44] U. Krämer, G.E.R. Schulze, Gittergeometrsiche Betrachtung der plastischen Verformung von Lavesphasen, Kristall und Technik 3 (3) (1968) 417–430.

[45] S. Zhang, Z. Xie, P. Keuter, S. Ahmad, L. Abdellaoui, X. Zhou, N. Cautaerts, B. Breitbach, S. Aliramaji, S. Korte-Kerzel, M. Hans, J. Schneider, C. Scheu, Atomistic structures of ⟨0001⟩ tilt grain boundaries in a textured Mg thin film, Nanoscale (2022), https://doi.org/10.1039/D2NR05505H.